Article

Stacking Fault Formation in LiNi$_{0.6}$Co$_{0.2}$Mn$_{0.2}$O$_2$ during Cycling: Fundamental Insights into the Direct Recycling of Spent Lithium-Ion Batteries

Kazuhiko Mukai*

Read Online

ACCESS | Metrics & More | Article Recommendations | SI Supporting Information

ABSTRACT: As the global marketplace for lithium-ion batteries (LIBs) proliferates, technologies for efficient and environmentally friendly recycling, i.e., direct recycling, of spent LIBs are urgently required. In this contribution, we elucidated the mechanisms underlying the degradation that occurs during the cycling of a Li/LiNi$_{0.6}$Co$_{0.2}$Mn$_{0.2}$O$_2$ (NCM622) cell. The results provided fundamental insights into the optimum procedures for direct recycling using a recently developed, state-of-the-art positive electrode material. Capacity fade in NCM622 was induced by cycling at high voltages above 4.6 V vs Li$^+$/Li, during which the rhombohedral symmetry approached cubic symmetry. The selective line broadening and peak shifts that appeared in the X-ray diffraction patterns after cycling indicated the formation of stacking faults along the c_h-axis. In addition, high-resolution transmission electron microscopy clarified that rock-salt domains were located on the NCM622 surface before and after cycling. These structural analyses confirmed that the NCM622 particles degrade not at their surfaces but rather in the bulk, contradicting previous reports where degradation during cycling is mainly caused by rock-salt domains on the surface. Material regeneration processes involving the restoration of the original stacking sequence are essential for effective direct recycling.
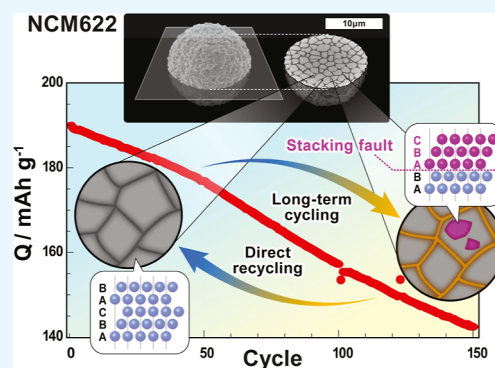
INTRODUCTION

Lithium-ion batteries (LIBs) have become an integral part of electric vehicles (EVs) in the more than 30 years since their commercialization in 1991.[1−3] In 2030, the sum of already-existing and newly registered EVs is expected to reach 250 million on the global marketplace, approximately ten times greater than that in 2020.[4,5] This rapid popularization of EVs will inevitably produce an enormous quantity of spent LIBs, which contain a certain amount (∼30 wt %) of valuable metals such as Li, Ni, Co, and Cu.[3−5] Sustainable and green recycling technologies for spent LIBs should therefore be established to make efficient use of limited metal sources.[4−8]

The valuable metals in freshly fabricated LIBs were originally produced from various mined ores through pyrometallurgy, hydrometallurgy, or both. Pyrometallurgy includes a high-temperature heating process (>∼ 800 °C) for reducing metal oxides to form alloys,[4,9] whereas hydrometallurgy consists of acid leaching and solvent extraction processes.[4,10] In principle, the valuable metals in spent LIBs can be recovered by these methods, which have advantages for mass production and the purity of the metals.[4−8] However, destruction-and-regeneration-type recycling consumes more total energy than that for producing these metals from ores and increases the risk of secondary environmental pollution; thus, many researchers have attempted to directly recycle these (positive) electrode materials

by simply reactivating them as a more efficient strategy for producing these materials.[11−14]

Direct recycling usually involves processes to recover the composition and structure of degraded positive electrode materials via relithiation and annealing.[11−14] For instance, Jiang et al.[11] regenerated degraded LiNi$_{0.5}$Co$_{0.2}$Mn$_{0.3}$O$_2$ (NCM523) by calcining at 850 °C for 12 h, followed by relithiation in eutectic molten salts of LiOH and Li$_2$CO$_3$. Meanwhile, Liu et al.[12] proposed a combination of oxalic acid leaching, relithiation, and annealing processes for degraded NCM523, wherein the oxalic acid leaching promoted the dissolution of Li$^+$ ions and the reduction of transition metals. Obviously, the optimum procedures for direct recycling depend on the use history of the battery and its degradation condition. Nevertheless, commercial spent LIBs with unknown backgrounds have been employed in most previous studies on direct recycling.[11−14] Therefore, to develop more effective strategies for direct recycling, it is crucial to elucidate the degradation

© 2023 The Author. Published by
American Chemical Society

mechanism of LIBs from the perspective of regeneration or reactivation.

In this study, we examined the relationship among capacity (Q), cyclability, and structural changes before and after cycling. We selected $LiNi_{0.6}Co_{0.2}Mn_{0.2}O_2$ (NCM622) as the model positive electrode material because the current trend in commercial LIBs is to shift toward materials with high nickel contents such as NCM622, $LiNi_{0.8}Co_{0.1}Mn_{0.1}O_2$ (NCM811), and $LiNi_{1-x-y}Co_xAl_yO_2$ (NCA) rather than those with moderate (NCM523) or low nickel contents such as $LiNi_{1/3}Co_{1/3}Mn_{1/3}O_2$ (NCM111).[15−17] Moreover, to exclude the contributions from the negative electrode,[18,19] we performed electrochemical cycling tests in a half cell using a Li metal electrode, thereby focusing on the degradation in the NCM622 electrode. Changes in the crystal structure and lattice parameters for the a_h- and c_h-axes from those in the initial state are essential for determining the properties of degraded electrodes, but previous results on NCM622 remain controversial.[20−23] For example, Wang et al.[20] and Jetybayeva et al.[23] claimed that it could be modeled as a single-phase material up to a cell voltage (E) of 4.6 V vs Li^+/Li, whereas Zhu et al.[22] proposed a two-phase model at $E \geq 3.78$ V. In addition, the Q dependences of a_h and c_h apparently differ, although these values were previously examined with respect to changes in E,[20,21] x in $Li_xNi_{0.6}Co_{0.2}Mn_{0.2}O_2$,[22] and the state of charge.[23] Previous studies on the structure of NCM622 utilized laboratory or synchrotron in situ X-ray diffraction (XRD),[20−23] which has limitations in determining the exact structural parameters and detecting minor phases due to narrow 2θ range and weak peak intensity of the XRD patterns. We thus conducted whole-powder pattern fitting analyses, i.e., Rietveld analyses, using ex situ synchrotron radiation XRD data before and after the cycling tests in different E ranges. Consequently, we revealed the presence of stacking faults along the c_h-axis in the degraded NCM622 samples, which probably formed during the process of transforming into a phase with cubic symmetry, particularly at $E \geq 4.4$ V. Possible procedures for reactivating the degraded NCM622 are also discussed.

EXPERIMENTAL SECTION

Materials Characterization. A sample of NCM622 powder was purchased from Hohsen Corp. and characterized by scanning electron microscopy (SEM; SU3500, Hitachi High-Technologies) and synchrotron radiation XRD analyses. We also obtained the powder samples of NCM111, NCM523, NCM811, and NCA ($LiNi_{0.88}Co_{0.09}Al_{0.03}O_2$) from Hohsen Corp. to compare NCM622 with other samples in terms of their electrochemical and structural properties. The XRD patterns were recorded at the BL5S2 beamline at the Aichi Synchrotron Radiation Center (Aichi SR) using a two-dimensional (2D) detector (PILATUS 100 K, Dectris). Approximately 2 mg of each sample was packed into a borosilicate glass capillary with a diameter of 0.3 mm (W. Müller Glas Technik) and exposed to X-rays for 10 min. The X-ray wavelength (λ) was determined to be 0.8000(2) Å using a silicon standard (NIST 640d). The Rietveld analysis was conducted using RIETAN-FP software,[24] and schematics of the crystal structures were drawn using VESTA software.[25]

Electrochemical Measurements. The electrochemical reactivities of NCM111, NCM523, NCM622, NCM811, and NCA were examined in a Li cell using an electrolyte of 1 M $LiPF_6$ dissolved in an ethylene carbonate (EC)/diethylene carbonate (DEC) mixture (EC/DEC = 1/1 by volume, Kishida Chemical). The working electrode consisted of 88 wt % active material, 6 wt

% conducting carbon (acetylene black; AB, HS-100, Denka), and 6 wt % polyvinylidene fluoride (PVdF, Kureha). A black slurry containing active material, AB, PVdF, and N-methyl-2-pyrrolidone (Nacalai Tesque) was cast onto an Al foil (=20 μm), dried in vacuum at 120 °C for 12 h, and finally cut into a disk with a diameter of 16 mm. The amount of active material in the electrode was ~14 mg. Lithium cells were fabricated in an Ar-filled glovebox (DBO-2BLKP, Miwa Mfg). A Li metal sheet pressed onto a stainless steel plate (diameter = 19 mm) was used as the counter electrode, while two sheets of a polypropylene membrane with a thickness of 25 μm (TonenGeneral Sekiyu) were used as the separator. The cells were cycled three times at a current of 0.3 mA ($\simeq 0.15$ mA cm^{-2}) in the range of 3.0−4.2 V. The temperature surrounding the cells was maintained at 25 °C by an incubator (MIR-254, PHC).

The cycling performance of NCM622 was investigated in seven different ranges: 3.0−3.9, 3.0−4.1, 3.0−4.2, 3.0−4.4, 3.0−4.6, 3.0−4.8, and 3.0−5.0 V. The procedures for preparing the electrodes and fabricating the Li cells were essentially the same as the aforementioned method. The cells were conditioned by cycling three times in the range 3.0−4.4 V at a current of 0.3 mA. Then, each cell was cycled 30 times in each voltage range at the same current. For only the range 3.0−4.4 V, an additional cell was cycled 150 times at a current of 0.3 mA, which took ~3 months until the end of the cycling.

To clarify the contributions from the degradation in the counter electrode, after the cycling tests, we replaced the Li electrode and separators with fresh ones in the Ar-filled glovebox. The cells were then cycled at 0.3 mA in the range 3.0−4.4 V. We also carried out cyclic voltammetry (CV) at a scan rate of 0.1 mA s^{-1} before and after the cycling test at 3.0−5.0 V.

Ex Situ XRD Measurements. Ex situ XRD patterns were recorded at the BL5S2 beamline at Aichi SR using the 2D detector (PILATUS 100 K, Dectris) and $\lambda = 0.8000(2)$ Å. Delithiated NCM622 samples were prepared by the electrochemical reaction; i.e., each Li cell was charged at a current of 0.3 mA to a desired Li composition at 25 °C, followed by a conditioning charge and discharge cycle in the range of 3.0−4.4 V. The NCM622 electrode was prepared using the same method as above. Each electrode was removed from the Li cell in the Ar-filled glovebox, then washed with DEC, and finally packed into a borosilicate glass capillary with a diameter of 0.5 mm (W. Müller Glas Technik). The charge capacities (Q_{cha}s) of the delithiated NCM622 samples were 25.0, 50.3, 78.2, 100.1, 125.6, 150.1, 175.2, 198.0, 216.0, 232.0, 238.6, and 243.5 mA h g^{-1}. Hereafter, we denote these samples as 25, 50, 78, 126, 150, 175, 198, 216, 232, 239, and 244 C.

Additionally, we performed ex situ XRD measurements after the cycling tests at 3.0−4.0, 3.0−4.2, 3.0−4.4 (30 cycles), 3.0−4.6, 3.0−4.8, 3.0−5.0, and 3.0−4.4 V (150 cycles). XRD data were recorded at the Aichi SR beamline Aichi 5S using the same 2D detector. Each electrode was packed into a borosilicate glass capillary with a diameter of 0.5 mm in the Ar-filled glovebox after washing the electrode with DEC. Rietveld analyses were conducted using RIETAN-FP software.[24]

TEM Analyses. Transmission electron microscopy (TEM; JEM-2100F, JEOL) analyses were conducted before and after cycling tests at 3.0−5.0 V. The TEM specimens were prepared using a dual-beam focused ion beam scanning microscope (Helios, FEI) with Ga ions at accelerating voltages from 2 to 40 kV. High-resolution TEM images were obtained at 200 kV using an objective lens with Cs = 0.5 mm. High-angle annular dark-
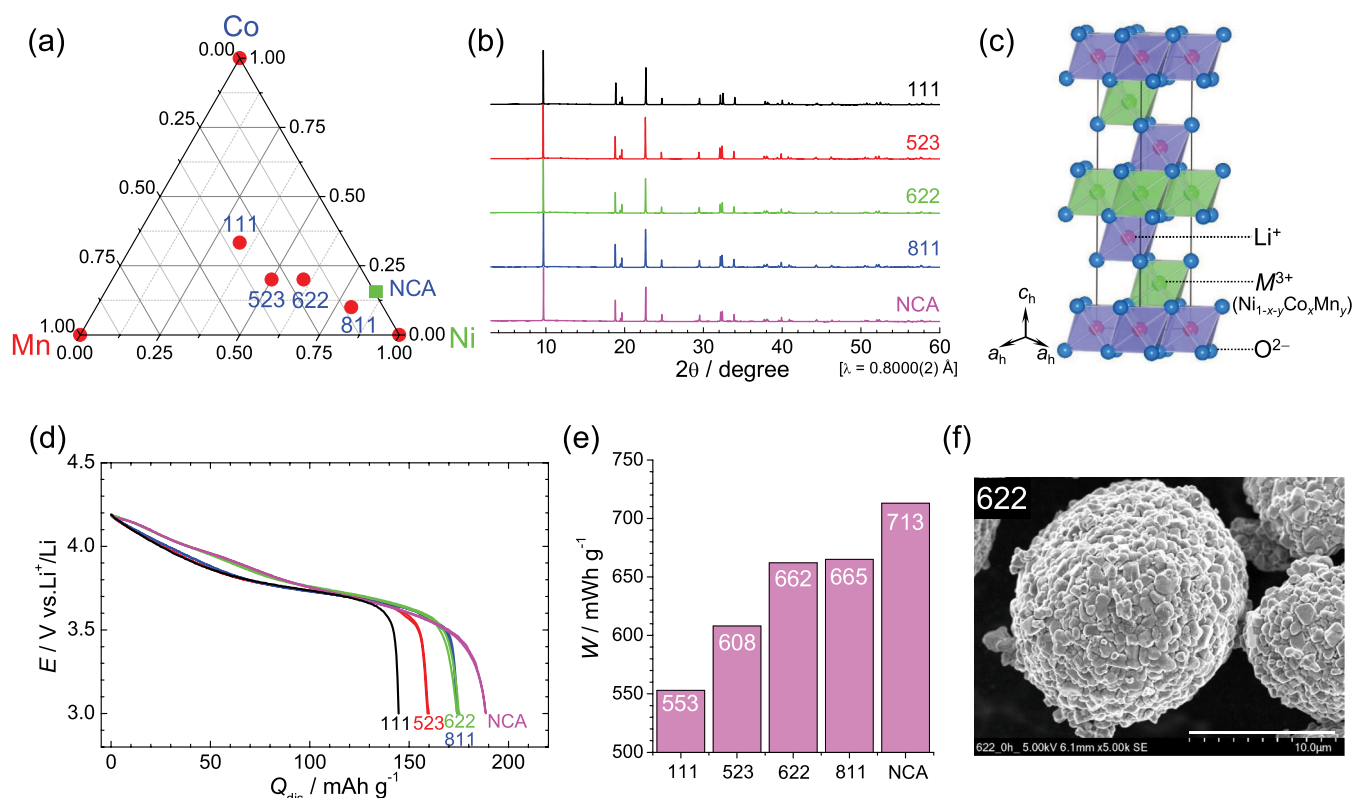
Figure 1. (a) Ternary phase diagram of $LiCoO_2-LiMnO_2-LiNiO_2$ and (b) synchrotron radiation XRD patterns of the NCM111, NCM523, NCM622, NCM811, and NCA samples. (c) Schematic of the layered structure for $LiMO_2$ (M = $Ni_{1-x-y}Co_xMn_y$) with the $R\overline{3}m$ space group. (d) Discharge curves of the Li cells with the NCM111, NCM523, NCM622, and NCA samples and (e) corresponding Ws. The cells were operated at 0.3 mA and 25 °C in the range of 3.0−4.2 V. (f) SEM image of the NCM622 particles.

field scanning TEM (HAADF-STEM) images were obtained with a convergence semiangle of 29 mrad and a collection angle of 75−200 mrad.

■ RESULTS AND DISCUSSION

Characterization of Present NCM622. First, we briefly describe the structural, electrochemical, and morphological characteristics of the NCM622 sample. As illustrated in Figure 1a, the NCM622 composition is located toward the lower right region of the ternary $LiCoO_2-LiMnO_2-LiNiO_2$ phase diagram, wherein a layered structure with rhombohedral ($R\overline{3}m$) symmetry is stable.[26] Figure 1b shows the synchrotron radiation XRD patterns of the NCM111, NCM523, NCM622, NCM811, and NCA samples. The crystal structure for all of the samples is assigned to the layered structure with the $R\overline{3}m$ space group, in which the Li^+, M^{3+} (=$Ni_{1-x-y}Co_xMn_y$), and the O^{2-} ions occupy $3b$, $3a$, and $6c$ sites, respectively (Figure 1c). The lattice parameters in the hexagonal setting were determined by the Rietveld analyses to be a_h = 2.8621(1) Å and c_h = 14.2458(1) Å for NCM111, a_h = 2.8696(1) Å and c_h = 14.2453(1) Å for NCM523, a_h = 2.8677(1) Å and c_h = 14.2190(1) Å for NCM622, a_h = 2.8734(1) Å and c_h = 14.2182(1) Å for NCM811, and a_h = 2.8728(1) Å and c_h = 14.2127(1) Å for NCA.

The a_h and c_h values of the present NCM622 sample are similar to the previously reported values.[20,21] The Rietveld analysis results are presented in further detail in the next section, together with those for the delithiated NCM622 samples. The Rietveld analysis results and structural parameters such as atomic positions and isotropic temperature factors (B_{iso}) for the other samples are provided in Figure S1 and Table S1.

Figure 1d shows the discharge curves of the Li cells with the NCM111, NCM523, NCM622, NCM811, and NCA samples starting above 4.2 V. Figure S2 shows the corresponding charge and discharge curves operated at 3.0−4.2 V. The discharge capacity (Q_{dis}) of NCM622 is ∼174 mA h g^{-1}, which is greater than the Q_{dis} of NCM111 ($\simeq$146 mA g^{-1}) and NCM523 ($\simeq$160 mA h g^{-1}) and similar to the Q_{dis} of NCM811 ($\simeq$174 mA h g^{-1}). Thus, the E value increases slightly with the increasing Ni content, particularly at $Q_{dis} \leq$ ∼100 mA h g^{-1}. Based on the average E during the discharge reaction, energy densities (Ws) of NCM111, NCM523, NCM622, NCM811, and NCA were calculated to be 553, 608, 662, 665, and 713 mW h g^{-1}, respectively (Figure 1e).

The NCM622 powder consists of large (10−20 μm) spherical primary particles with diameters of ∼1 μm (Figure 1f). This particle shape is common among NCM- and NCA-based materials, although NCM622 compounds consisting of large, isolated primary particles with diameters of 2−5 μm were recently proposed to improve the cyclability.[27,28]

***Ex Situ* XRD Measurements.** As described in the Introduction, changes in the crystal structure of NCM622 have not yet been clarified, even in the initial state.[20−23] Hence, we recorded *ex situ* XRD patterns from the delithiated NCM622 samples before investigating the cycling performance in various voltage ranges. Figure 2a shows typical conditioning charge and discharge curves of the Li/NCM622 cell for the *ex situ* XRD measurements. The cell was operated at a current of 0.3 mA in the range of 3.0−4.4 V. Stable charge and discharge curves are observed, except for the charge curve of the first cycle, during which the electrolyte decomposes at the Li (counter) electrode.
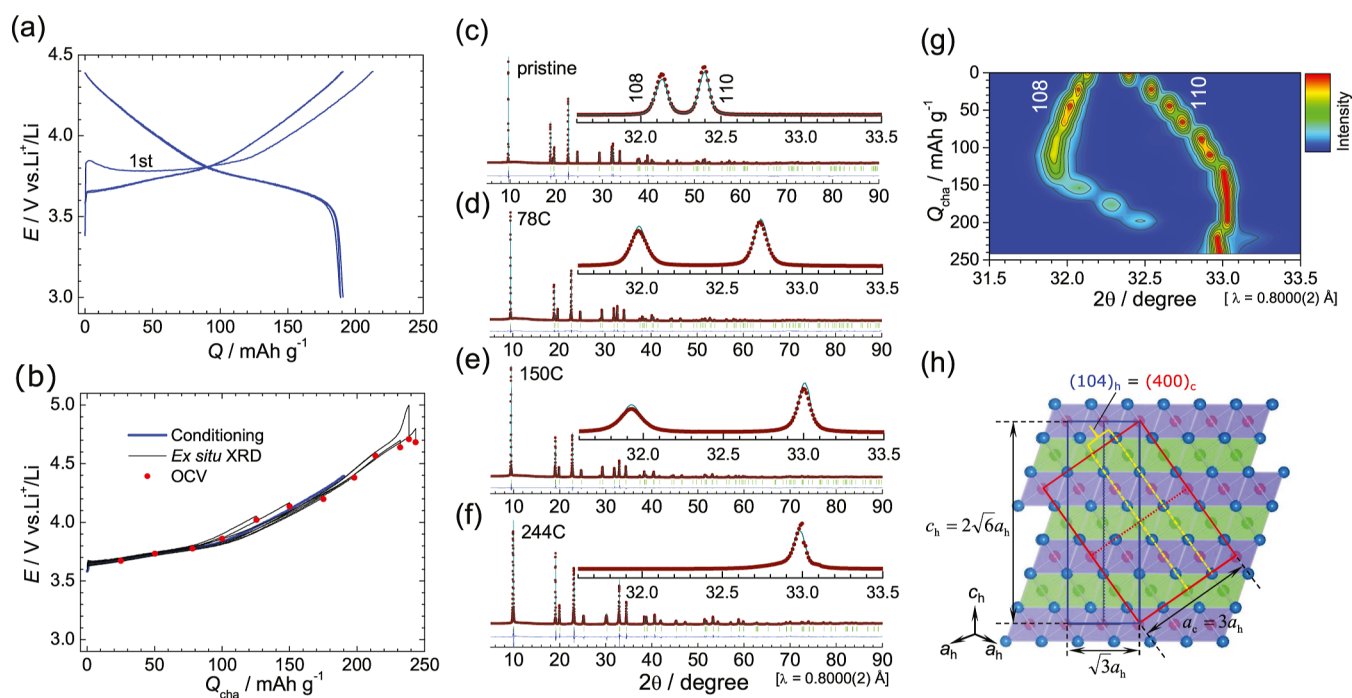
Figure 2. (a) Conditioning charge and discharge curves of the Li/NCM622 cell operated at 3.0−4.4 V. (b) Charge curves (black lines) and OCVs (red circles) for the *ex situ* XRD measurements. The conditioning charge curve from the last cycle (blue line) is also shown for comparison. Rietveld analysis results of the (c) pristine, (d) 78 C, (e) 150 C, and (f) 244 C samples together with the enlarged 108 and 110 diffraction peaks. (g) Contour plots of the 108 and 110 diffraction peaks during the charge reaction. (h) Crystal relationship between rhombohedral and cubic symmetries viewed from the [110] direction in the rhombohedral symmetry. When $c_h/a_h = 2\sqrt{6}$, the rhombohedral structure is converted into the cubic (FCC) structure with $a_c = 3a_h$. The unit cells of the rhombohedral and cubic structures are shown by the blue and red solid lines, respectively. The (104) plane in the rhombohedral structure corresponds to the (400) plane in the cubic structure.

Table 1. a_h and c_h Values of the NCM622 Samples in the Initial State Obtained by *Ex Situ* XRD Measurements

sample	Q_{cha}/mA h g^{-1}	x in Li$_x$Ni$_{0.6}$Co$_{0.2}$Mn$_{0.2}$O$_2$	OCV/V	a_h/Å	c_h/Å	c_h/a_h
pristine	0	1		2.8677(1)	14.2190(1)	4.9583(1)
25 C	25.0	0.91	3.670	2.8556(1)	14.2919(1)	5.0048(1)
50 C	50.3	0.82	3.731	2.8458(1)	14.3538(2)	5.0439(1)
78 C	78.2	0.72	3.774	2.8388(1)	14.3965(2)	5.0713(1)
100 C	100.1	0.64	3.860	2.8284(1)	14.4564(3)	5.1112(1)
126 C	125.6	0.54	4.019	2.8241(1)	14.4838(3)	5.1287(1)
150 C	150.1	0.46	4.135	2.8165(1)	14.4937(3)	5.1460(1)
175 C	175.2	0.36	4.200	2.8147(1)	14.4003(4)	5.1161(1)
198 C	198.0	0.28	4.379	2.8142(1)	14.2603(3)	5.0673(1)
216 C	216.0	0.22	4.467	2.8129(1)	14.1146(2)	5.0178(1)
232 C	232.0	0.16	4.638	2.8138(1)	14.0534(3)	4.9945(1)
239 C	238.6	0.13	4.708	2.8182(1)	13.6793(3)	4.8539(1)
244 C	243.5	0.12	4.681	2.8167(1)	13.7820(4)	4.8930(1)

Figure 2b shows the charge curves (black lines) for delithiating the NCM622 samples for the *ex situ* XRD measurements. The charge curves almost trace the conditioning charge curve (blue line), indicating a homogeneous and reproducible electrochemical reaction
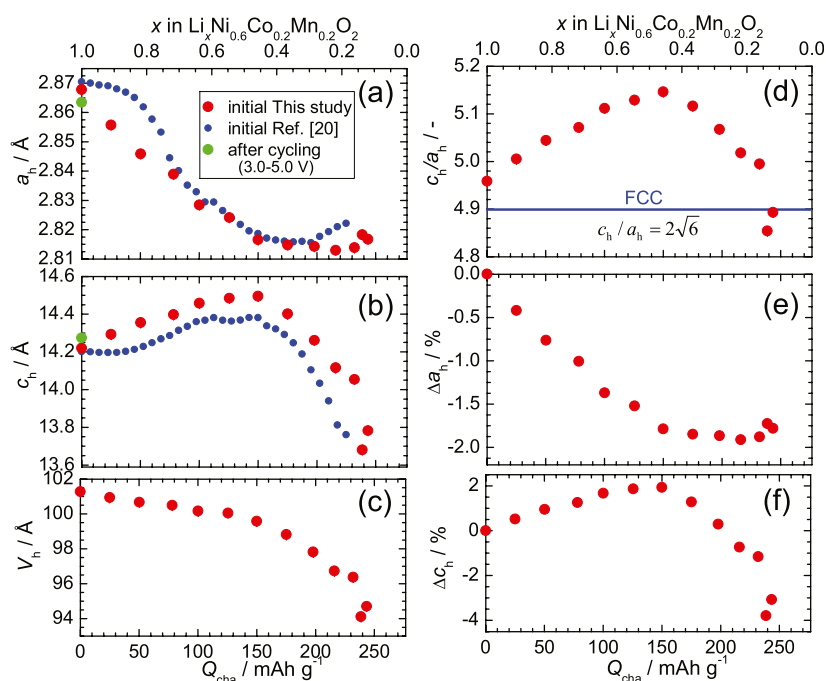
$$LiNi_{0.6}Co_{0.2}Mn_{0.2}O_2$$
$$\rightarrow (1-x)Li^+ + (1-x)e^- + Li_xNi_{0.6}Co_{0.2}Mn_{0.2}O_2 \tag{1}$$
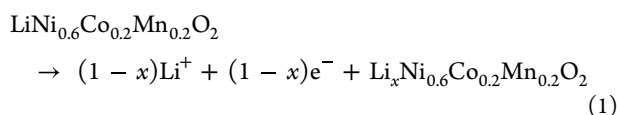
with a theoretical capacity (Q_{theo}) of 276.5 mA h g^{-1}. Table 1 lists the Q_{cha}, open-circuit voltage (OCV), and x for the *ex situ* XRD measurements, where x is calculated as $1 - Q_{cha}/Q_{theo}$.

Figure 2c−f shows the Rietveld analysis results of the pristine, 75, 150, and 244 C samples, respectively. Figures S2 and S3

show the Rietveld analysis results of other delithiated NCM622 samples, and Figures S2 and S3 list the structural parameters of all the samples. The delithiated samples can be assigned to a single phase with the $R\bar{3}m$ space group until 244 C ($x = 0.12$), although previous *in situ* XRD studies on NCM622 limited the charge voltage to 4.6 V[20] or 4.5 V,[21] $x = 0.35$,[22] or $Q_{cha} = 150$ mA h g^{-1}.[23] NCM622 differs from Li$_x$CoO$_2$[29,30] and Li$_x$NiO$_2$;[31] for example, at least four different layered phases were observed in Li$_{0.1}$NiO$_2$.

As shown in the insets of Figure 2c−f, the 108 and 110 diffraction peaks shift toward opposite diffraction angles with increasing Q_{cha}, and finally, the 108 diffraction peak disappears at 244 C. The Q_{cha} dependence of these peak changes is visualized in the contour plot of the 108 and 110 diffraction peaks shown in

Figure 3. Changes in (a) a_h, (b) c_h, (c) V_h, (d) c_h/a_h, (e) Δa_h, and (f) Δc_h in the initial state. x in $Li_xNi_{0.6}Co_{0.2}Mn_{0.2}O_2$ was calculated by $1 - Q_{cha}/Q_{theo}$; *i.e.*, we ignored the contribution from the irreversible capacity in the first cycle. Previous a_h and c_h values,[20] which were deduced from the original E dependence of the a_h and c_h data, are shown in (a,b) for comparison. The solid line in (d) represents the c_h/a_h ratio (=2 $\sqrt{6}$) when the rhombohedral structure converts into the cubic (FCC) structure.
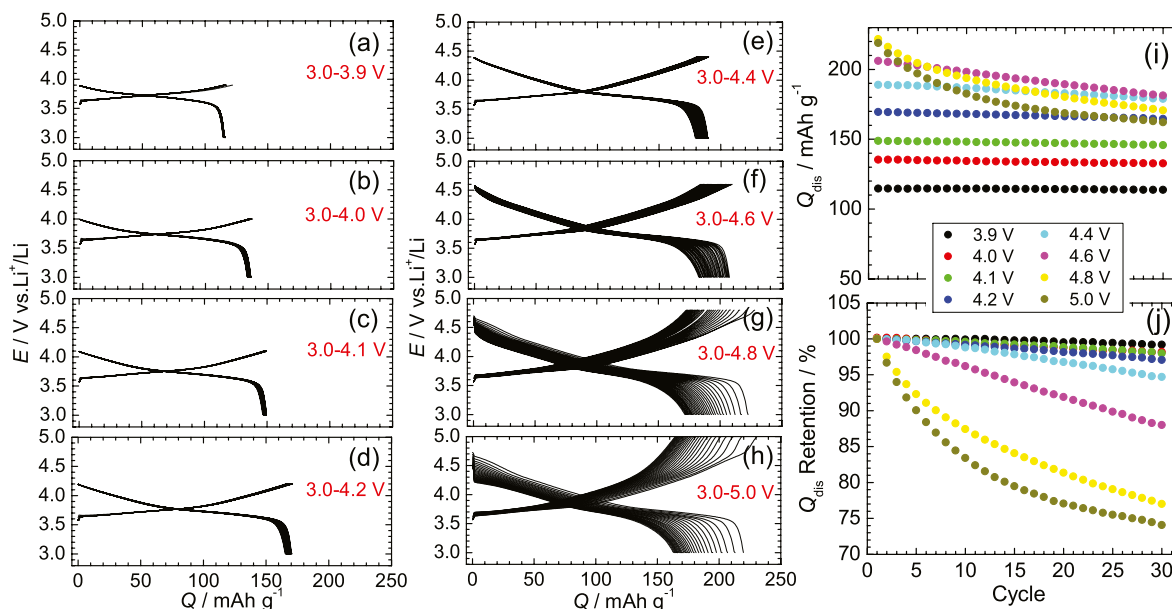

Figure 4. Charge and discharge curves of the Li/NCM622 cells operated at a current of 0.3 mA in the ranges of (a) 3.0−3.9 V, (b) 3.0−4.0 V, (c) 3.0−4.1 V, (d) 3.0−4.2 V, (e) 3.0−4.4 V, (f) 3.0−4.6 V, (g) 3.0−4.8 V, and (h) 3.0−5.0 V. Corresponding (i) Q_{dis} and (j) Q_{dis} retention as functions of the cycle number.

Figure 2g. The difference in the 2θ angle between the 108 and 110 diffraction peaks reaches a maximum at $Q_{cha} \simeq 140$ mA h g^{-1} (~1.1°); thereafter, the 108 diffraction peak becomes closer to the 110 diffraction line, and its intensity decreases.

According to the crystal relationship between the rhombohedral and cubic symmetries, the rhombohedral structure converts to the cubic (face-centered-cubic, FCC) structure when $c_h/a_h = 2\sqrt{6}$ (Figure 2h). In this structure, the cubic lattice parameter (a_c) equals $3a_h$. Moreover, the 104 diffraction peak in the

rhombohedral structure corresponds to the 400 diffraction peak in the cubic structure, while the 110 diffraction peak in the rhombohedral structure transforms to the 440 diffraction peak in the cubic structure. Therefore, the changes in the 108 and 110 diffraction peaks at $Q_{cha} > 140$ mA h g^{-1} indicate that the rhombohedral crystal structure approaches the cubic structure.

Figure 3a−c shows changes in a_h, c_h, and the unit cell volume (V_h), respectively, during the charge reaction, and Table 1 lists the absolute a_h and c_h values. The a_h value decreases almost
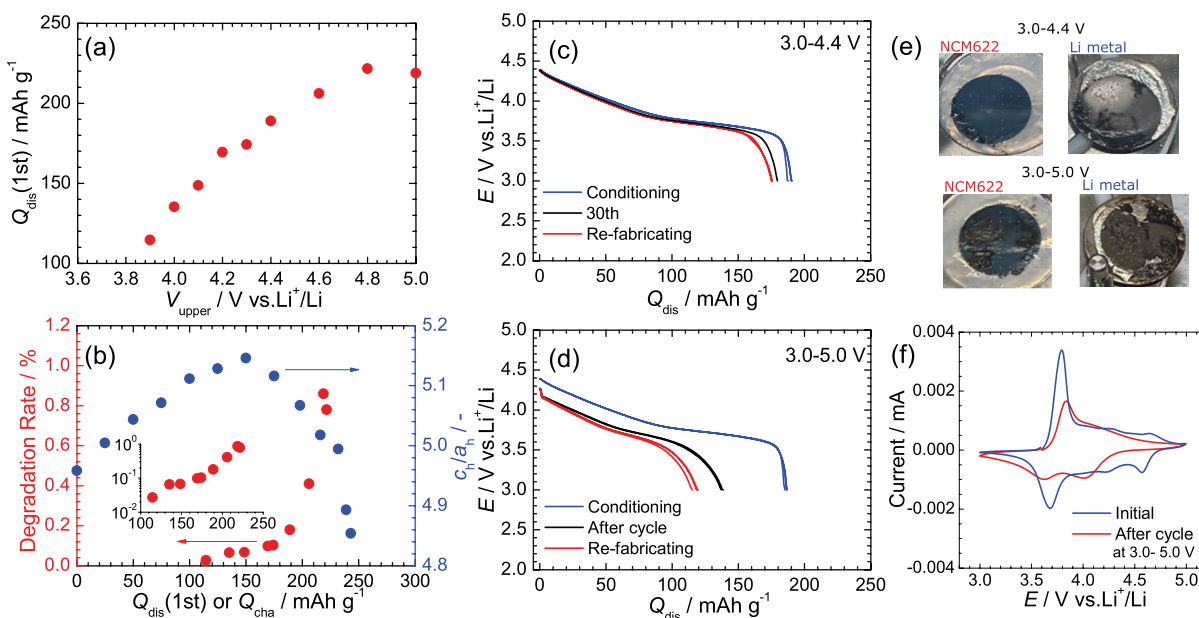
Figure 5. (a) Q_{dis} (first) as a function of V_{upper}. (b) Q_{dis} (first) dependence of the degradation rate (left axis) and Q_{cha} dependence of c_h/a_h (right axis). The inset in (b) shows the semilog plot of Q_{dis} (first) vs degradation rate. (c) Comparison of the discharge curves of the Li/NCM622 cell during the conditioning cycle, the 30th cycle during the cycling test, and after refabrication. The cell was operated at 3.0−4.4 V throughout the measurements. (d) Comparison of the discharge curves of the Li/NCM622 cell during the conditioning cycle, after the cycling test but before refabrication, and after refabrication. (e) Photos of the NCM622 and Li electrodes after the cycling tests at 3.0−4.4 V (upper) and 3.0−5.0 V (bottom). (f) CV curves before and after testing at 3.0−5.0 V for 30 cycles.

linearly from 2.8677(1) Å at 0 mA h g^{-1} to 2.8165(1) Å at 150.1 mA h g^{-1} and then remains constant $(\sim2.815$ Å$)$ until the end of the charge reaction. Meanwhile, the c_h value increases from 14.2190(1) Å at 0 mA h g^{-1} to 14.4937(3) Å at 150.1 mA h g^{-1} and then rapidly drops to $\sim$13.7 Å at $\sim$240 mA h g^{-1}. Because $V_h = \sqrt{3}\, a_h^2 \times c_h$, V_h decreases with Q_{cha}, although its slope changes. The trends in a_h, c_h, and V_h with Q_{cha} can be considered common for layered materials such as NCM622,[20] Li$_x$CoO$_2$,[29,30] and Li$_x$NiO$_2$.[31] However, in Figure 3a,b, the differences clearly appear between the results of present and previous[20] studies on NCM622 for a_h at $Q_{cha} < 80$ mA h g^{-1} and in the entire c_h region. More specifically, the maximum c_h (c_h^{max}) in the previous study was $\sim$14.38 Å,[20] which is slightly lower than typical c_h^{max} values $(\simeq14.5$ Å$)$ for layered materials.[29−31] This is probably because these previous a_h and c_h values were obtained through laboratory *in situ* XRD measurements,[20] which include inhomogeneities or different microstructures in the electrode due to difficulties in the reproduction of intrinsic electrochemical properties of NCM622 during the *in situ* measurements.

Figure 3d−f shows the changes in c_h/a_h, Δa_h, and Δc_h, respectively, where Δa_h (or Δc_h) represents the ratio relative to the initial a_h (or c_h). The Q_{cha} dependence of c_h/a_h resembles the Q_{cha} dependence of c_h; namely, c_h/a_h increases from 4.958(1) at 0 mA h g^{-1} to 5.146(1) at 150.1 mA h g^{-1} and then rapidly drops to $\sim$4.90 at $\sim$240 mA h g^{-1}. Because $c_h/a_h = 2\sqrt{6}$ is the condition for the cubic structure, only 239 C possesses cubic symmetry, whereas the other samples delithiated at $Q_{cha} > 150$ mA h g^{-1} crystallize into the rhombohedral or pseudocubic symmetry. As illustrated by Figure 3e,f, Δc_h varies to a wider degree than Δa_h. On the boundary of $\sim$150 mA h g^{-1}, Δc_h suddenly decreases from approximately +2.0% to approximately −4% at the end of the charge reaction.

Relationship between Structural Changes and Cyclability. Keeping in mind the observed structural changes with

Q_{cha}, we performed cycling tests over various voltage ranges. Figure 4a−h shows the charge and discharge curves of the Li/NCM622 cells in the ranges of 3.0−3.9, 3.0−4.0, 3.0−4.1, 3.0−4.2, 3.0−4.4, 3.0−4.6, 3.0−4.8, and 3.0−5.0 V, respectively. The applied current was 0.3 mA for all of the Li/NCM622 cells. Because the amount of the NCM622 sample was $\sim$14 mg in each electrode, the C-rate was calculated to be $\sim$0.1 C for the cycling test at 3.0−5.0 V. Although Q_{dis} increases with the upper charge voltage (V_{upper}), it decreases with each cycle, particularly at $V_{upper} \geq 4.6$ V. Figure 4i shows Q_{dis} as a function of the number of cycles, and the corresponding Q_{dis} retention rate is shown in Figure 4j. At the 30th cycle, more than 95% of Q_{dis} is retained at $V_{upper} \leq 4.4$ V, whereas less than 80% remains at $V_{upper} \geq 4.8$ V, although the degradation rate gradually decreases with the cycle number.

Figure 5a shows the V_{upper} dependence of Q_{dis} for the first cycle $[Q_{dis}(first)]$. As mentioned above, $Q_{dis}(first)$ increases from 114.6 mA h g^{-1} at $V_{upper} = 3.9$ V to 188.9 mA h g^{-1} at $V_{upper} = 4.4$ V and then remains $\sim$220 mA h g^{-1} at $V_{upper} \geq 4.8$ V. The degradation rate (*i.e.*, the percentage decrease per cycle) rapidly increases at $Q_{dis}(first) > 200$ mA h g^{-1} (Figure 5b, left axis). As shown in the inset of Figure 5b, the degradation rate has a logarithmic relation with Q_{dis} (first). Figure 5b also shows the Q_{cha} dependence of c_h/a_h on the right axis, revealing that the degradation rate corresponds to the rapid decrease in c_h/a_h.

We then disassembled the Li cells in the Ar-filled glovebox and refabricated the Li cells using fresh Li electrodes, separators, and electrolyte. Figure 5c compares the discharge curves of the Li/NCM622 cell during the conditioning step, the 30th cycle during the cycling test, and after refabrication. This cell was operated at 3.0−4.4 V throughout the measurements. Additionally, Figure 5d shows the discharge curves of the Li/NCM622 cell during the conditioning cycle, after the cycling test but before refabrication, and after the refabrication. This cell was operated at 3.0−4.4 V, except for the cycling test at 3.0−5.0
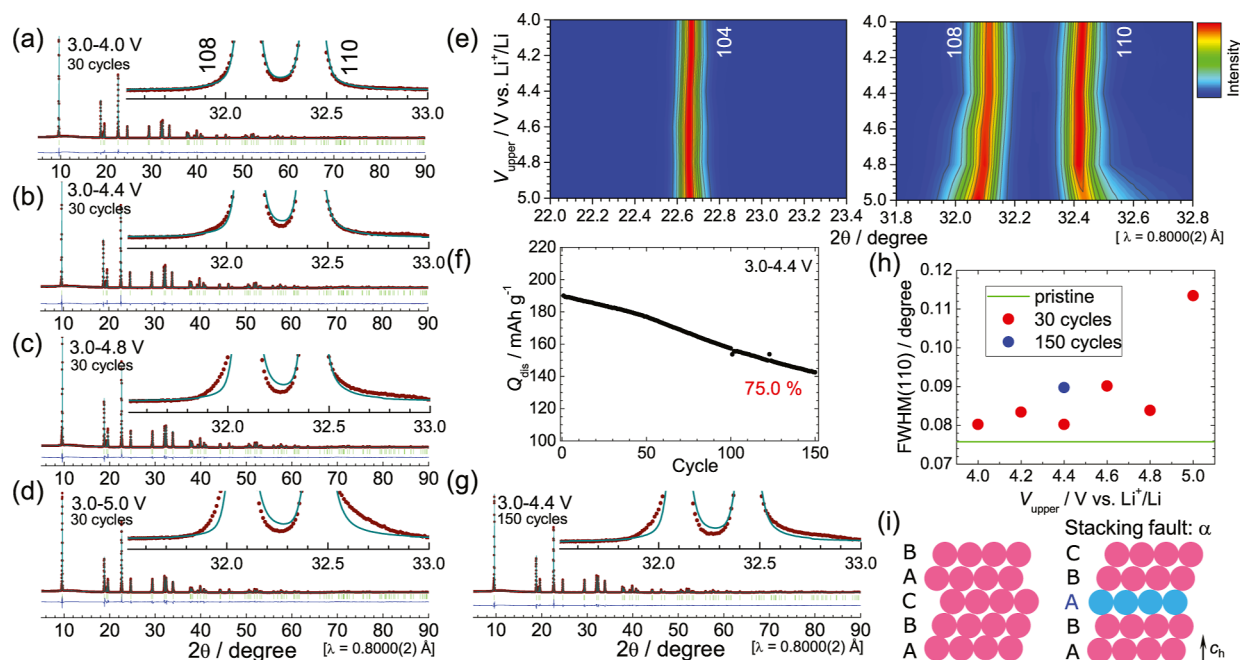
Figure 6. Rietveld analysis results after cycling tests (30 cycles) at (a) 3.0−4.0 V, (b) 3.0−4.4 V, (c) 3.0−4.8 V, and (d) 3.0−5.0 V. Insets show the XRD patterns enlarged near the 108 and 110 diffraction peaks. Closed circles and solid lines indicate the observed and calculated XRD data, respectively. (e) Contour plots of the 104, 108, and 110 diffraction peaks at $4.0 \leq V_{upper} \leq 5.0$ V. (f) Cycling performance of the Li/NCM622 cell operated for 150 cycles at a current of 0.3 mA and 3.0−4.4 V and (g) its Rietveld analysis results after the cycling test. (h) V_{upper} dependence of the fwhm of the 110 diffraction peaks after cycling 30 and 150 times. (i) Schematic of the ideal FCC packing of ABCAB··· and packing with an ABABC··· stacking fault.

V for 30 cycles. Q_{dis} decreases to ~180 from ~189 mA h g^{-1} during the cycling test at 3.0−4.4 V and then slightly decreases to ~177 mA h g^{-1} after refabrication. Meanwhile, Q_{dis} decreases to ~137 from ~187 mA h g^{-1} after the cycling test at 3.0−5.0 V and then further decreases to ~118 mA h g^{-1} after refabrication. Moreover, E drops to ~4.2 V at the beginning of the discharge reaction, indicating an increase in the internal resistance of the Li cell. As shown in Figure 5e, the surfaces of the Li metal electrodes are severely oxidized and turn black after the cycling tests at 3.0−4.4 and 3.0−5.0 V. Each separator contains these black decomposition products at the sides of the Li metal electrode. Because Q_{dis} did not recover even when employing a fresh Li electrode, separators, and electrolyte, the origins of the decrease in Q_{dis} are mainly considered to be the degradation of the NCM622 electrode. Indeed, the CV curve after the cycling test at 3.0−5.0 V exhibits broad, weak anodic (or cathodic) peaks, suggesting structural changes after the cycling test.

Structural Changes after Cycling Tests. We next examined the structural changes after cycling tests through XRD and TEM analyses. Figure 6a−d shows the Rietveld analysis results after the cycling tests at 3.0−4.0, 3.0−4.4, 3.0−4.8, and 3.0−5.0 V, respectively, while the Rietveld analysis results after the cycling tests at 3.0−4.2 and 3.0−4.6 V are shown in Figure S5. All the XRD patterns can be assigned to the layered structure with the $R\bar{3}m$ space group without any impurities such as a rock-salt NiO phase. As listed in Table 2, the a_h values after the cycling tests are slightly lower than those of the pristine a_h, while the c_h values are slightly larger than those of the pristine c_h. This indicates a deficiency of Li$^+$ ions from the stoichiometric ratio, although we fixed the occupancy of Li$^+$ ions to 1 in the Rietveld analyses (Table S5). The a_h and c_h values after the cycling test at 3.0−5.0 V are represented by green closed circles in Figure 3a,b for comparison.

Table 2. Lattice Parameters of the NCM622 Electrodes after the Cycling Tests

cycle	voltage range/V	a_h/Å	c_h/Å
30 cycles	3.0−4.0	2.8649(1)	14.2406(2)
	3.0−4.2	2.8654(1)	14.2395(2)
	3.0−4.4	2.8659(1)	14.2367(2)
	3.0−4.6	2.8656(1)	14.2478(2)
	3.0−4.8	2.8659(1)	14.2506(2)
	3.0−5.0	2.8634(1)	14.2735(3)
150 cycles	3.0−4.4	2.8645(1)	14.2515(2)

The insets of Figure 6a−d show the XRD patterns enlarged near the 108 and 110 diffraction peaks. The calculated XRD patterns (solid lines) almost reproduce the experimentally observed ones (closed circles) after the cycling tests at 3.0−4.0 and 3.0−4.4 V, whereas the two XRD patterns begin to differ after the cycling tests at 3.0−4.8 and 3.0−5.0 V. Specifically, the 108 diffraction peak shifts toward lower angles with a growing shoulder toward lower angles, while the 110 diffraction peak shifts toward higher angles with a growing shoulder toward higher angles (see the inset of Figure 6d). As can be understood from the XRD patterns enlarged near other diffraction peaks (Figure S6), three types of differences occur between the calculated and observed XRD patterns: (i) almost no difference, such as the 003 diffraction peak, (ii) shifts toward lower angles, such as the 108 and 1011 (Figure S6c) diffraction peaks, and (iii) shifts toward higher angles such as the 101 and 110 diffraction peaks. Figure 6e shows the contour plots of the 104, 108, and 110 diffraction peaks to visualize the V_{upper} dependence of the differences between the calculated and observed XRD patterns. The 108 and 110 diffraction peaks shift toward lower and higher angles with V_{upper}, respectively, whereas the 104 diffraction peak remains constant at ~22.7°.
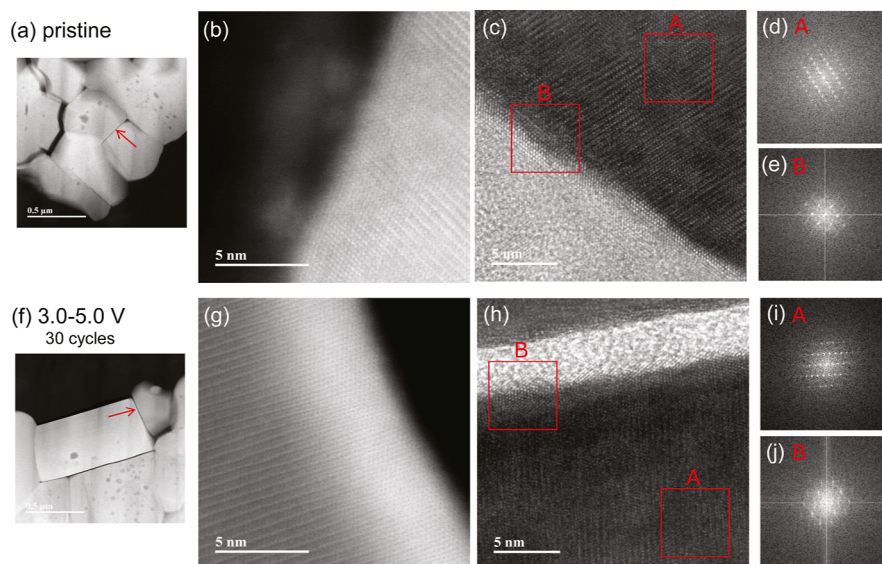
Figure 7. (a) Dark-field STEM image, (b) HAADF-STEM image, (c) high-resolution TEM image, and FFTs from the marked region of (d) A (bulk) and (e) B (surface) in (c) of the pristine NCM622 sample. (f) Dark-field STEM image, (g) HAADF-STEM image, (h) high-resolution TEM image, and FFTs from the marked region of (i) A (bulk) and (j) B (surface) in (h) of the cycled NCM622 sample at 3.0−5.0 V. The red arrows in (a,f) indicate the regions observed by HAADF-STEM in (b) and (g), respectively.

Because the increase in V_{upper} induced large structural changes in c_h/a_h and Δc_h, particularly above 4.6 V (Figure 3d,f), we next examined the structural changes after extended cycling tests with a limited V_{upper}. Figure 6f shows the cycling performance of the Li/NCM622 cell after operating for 150 cycles in the range 3.0−4.4 V. The applied current was 0.3 mA, and the cycling test lasted approximately three months. The Q_{dis} retention at the 150th cycle was 75.0%, which eventually became similar to that for the cycling test at 3.0−5.0 V for 30 cycles (Figure 4j). Figure 6g shows the Rietveld analysis result after this cycling test together with the XRD patterns enlarged near the 108 and 110 diffraction peaks. Differences appear in the observed and calculated XRD patterns for both diffraction peaks, suggesting a common degradation mechanism in the high-V_{upper} and long-term cycling tests.

Figure 6h shows the full-width at half-maximum (fwhm) of the 110 diffraction peak after the cycling tests at 4.0 V ≤ V_{upper} ≤ 5.0 V for 30 and 150 cycles. The fwhm value increases from that of the pristine NCM622 sample indicated by the green solid line ($\simeq 0.075°$) with V_{upper} or the cycle number. The peak shifts and the increase in the fwhm of the diffraction peaks can be interpreted as being due to the formation of the stacking faults in the lattice, which have been reported for various alloys with the FCC structure.[32−34] As for the present NCM622 case, there are three types of differences in the diffraction peaks in these compounds.[32−34] For instance, the diffraction peaks with $h + k + l = 3n + 1$ shift toward higher angles,[32−34] where hkl is the Miller index of the FCC structure.

Figure 6i illustrates a stacking fault included in the ABCAB⋯ packing sequence of the FCC structure, which corresponds to the direction of the c_h-axis in the rhombohedral structure. There are several types of stacking faults;[35] for instance, AB(A)-BCABC⋯, AB(A)CABCA⋯, and AB(A)CBACB⋯, which are classified as deformation (intrinsic), extrinsic, and growth (twin) stacking faults, respectively (see Figure S7). When α is the probability of a fault occurring at any layer, $1 - \alpha$ is the probability of the regular stacking sequence, *i.e.*, the probability of A being followed by C, B being followed by A, and C being

followed by C. According to the Paterson's model[32,33] on scattering amplitudes for layers including α, the normalized peak profile (I) at the peak position of (l_H) is represented by

$$I = \frac{\frac{3}{2}\alpha(1 - \alpha)}{1 - \frac{3}{2}\alpha(1 - \alpha) - [1 - 3\alpha(1 - \alpha)]^{1/2} \cos 2\pi\left(\frac{l_H}{3} + \frac{1}{2} \pm \phi/2\pi\right)} \quad (2)$$

where

$$\phi = \arctan[\sqrt{3}(1 - 2\alpha)] \quad (3)$$

The difference in the fwhm $(\Delta 2\theta)$ is thus related to

$$\Delta 2\theta = \frac{3\alpha|h + k + l|\tan\theta}{2(h^2 + k^2 + l^2)} \quad (4)$$

The α values are estimated to be 0.3 and 0.09 after the cycling tests at 3.0−5.0 and 3.0−4.4 V (for 150 cycles), respectively, if we employ the above consideration to the present case. Recently, one of structural refinement programs, FAULTS,[36] has been utilized to examine broadening of superlattice diffraction peaks in $Na_3Ni_2BiO_6$[37] and Na_2RuO_3,[38] which are applied to a positive electrode material for an Na-ion battery. Both Paterson's model and FAULTS originally deal with the 2D crystals containing planar defects, which have been tackled by Landau, Lifshitz, and Wilson *etc.*[32,33,36,39] The selective peak shift after cycling is another indicator for determining α in NCM622 but it is valid only for materials with the FCC structure.[32,33] Further experiments on cycled LIB materials such as $LiMn_2O_4$ as well as comparison between several structural refinement methods are required to elucidate the formation mechanism of stacking faults during cycling.

Figure 7a−c shows the results of the TEM analyses of the pristine NCM622 sample, namely, a dark-field STEM, HAADF-STEM, and high-resolution TEM images, and Figure 7d,e is the fast Fourier transforms (FFTs) of the regions labeled A (bulk) and B (surface) in Figure 7c, respectively. Similarly, Figure 7f−j shows the analogous TEM images and FFTs recorded after the cycling test at 3.0−5.0 V. Figure S8 shows enlarged dark-field
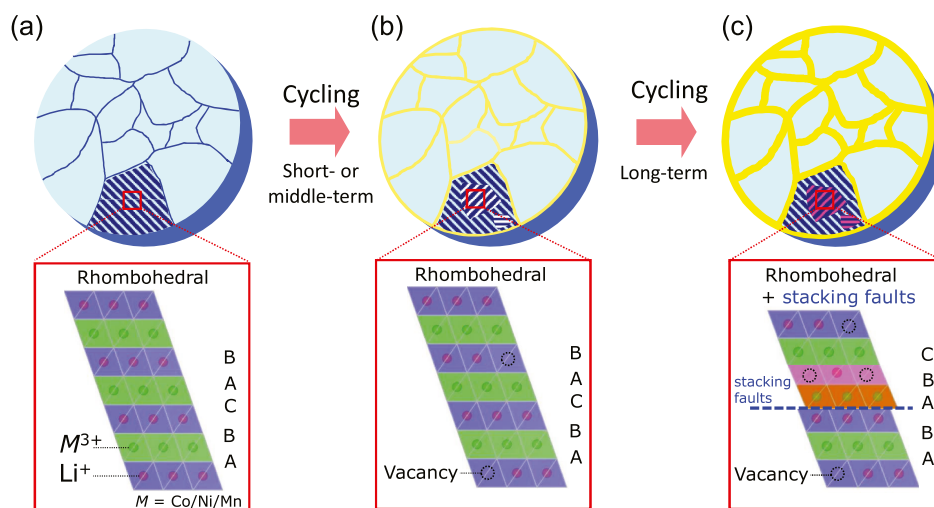
Figure 8. Schematic of the degradation mechanism during cycling. NCM622 particle in the (a) initial, (b) short- or middle-term, and (c) long-term stages of cycling. The shaded lines in the primary particles indicate the direction of crystallites, while the yellow lines between the primary particles correspond to the CEI.

STEM images of the pristine and cycled NCM622 samples. The individual primary particles adhere to one another even after the cycling test (Figure S8), although internal microcracks were previously observed for cycled NCM811[21] and fully charged NCA[40] compounds.

In the HAADF-STEM image of the cycled sample (Figure 7g), the surface appears white, which is consistent with the fact that a_h [=2.8634(1) Å] and c_h [=14.2735(3) Å] values after the cycle test were slightly different from those for initial values (see Figure 3a,b). The FFTs from region A in both samples can be assigned to the diffraction pattern from the [100] direction of the $R\bar{3}m$ space group. In contrast, FFTs from region B for both samples can be assigned to the diffraction pattern from the [110] direction of the $Fm\bar{3}m$ space group. A difference in the diffraction patterns between the surface and bulk has been reported for cycled NCM811 compounds.[21,41] However, as the rock-salt phase was observed even in the pristine NCM622 sample, this phase is probably not related to degradation during cycling. Moreover, the rock-salt phase is easily produced by repeated electron irradiation because this material is highly susceptible to electron beam damage, thus complicating the distinction between the structural changes during cycling and changes caused by beam damage.[42] Although the reason behind tracers for stacking faults not being observed in the TEM analyses is currently unclear, the resolution of HAADF-STEM is thought to be one of the possibilities for this absence. This is because atomic-resolution HAADF-STEM reveals the presence of stacking faults in a LiMn$_2$O$_4$ epitaxial film.[43]

Degradation Mechanism and Strategies for Direct Recycling. Based on the obtained results, Figure 8 summarizes the degradation mechanism of the NCM622 sample during cycling. The regular stacking sequence with the ABCABC packing is maintained during short- and middle-term cycling (Figure 8b), but stacking faults such as ABABC packing deteriorate the sample after long-term cycling (Figure 8c). Note that fewer stacking faults (α) exist after the cycling test at 3.0−4.4 V (150 cycles) than that after the cycling test at 3.0−5.0 V (30 cycles), although the Q_{dis} retention was similar between two cycling tests. This indicates the presence of noncrystalline decomposition products on the surface between the primary particles (indicated by yellow lines in Figure 8b,c), which have

recently been recognized as a "cathode electrolyte interphase (CEI)".[44,45] Otherwise, oxygen evolution from the NCM622 lattice participates in the degradation at high voltages above 4.4 V, as in the case for LiNiO$_2$.[46]

The stacking faults are presumed to originate as follows. The rhombohedral symmetry approaches cubic symmetry during the charge reaction with a decrease in c_h/a_h above ~150 mA h g^{-1}. When the cubic symmetry returns to the rhombohedral symmetry during the discharge reaction, the structure changes in four different directions because cubic symmetry possesses four 3-fold axes. Thus, as shown in Figure 8a−c, the stacking faults are produced during cycling, followed by the formation of randomly oriented crystallites in the NCM622 particles. The neighborhood around such stacking faults is electrochemically inactive, thus decreasing Q_{cha} and Q_{dis}.

High-temperature annealing would be required to rearrange the stacking sequence back into its original form because the degraded region is located in the interior of the primary particles. The stacking fault energies reported for various alloys[34] would be helpful for exploring the optimum heating conditions for material regeneration. According to previous studies on direct recycling for NCM523 compounds,[11,14] the peak intensity ratio of the 104 diffraction peak to the 003 diffraction peak, I_{104}/I_{003}, increased after unspecified degraded process, confirming the occupancy of metal ions (Ni, Co, and Mn) in the Li layer. Indeed, the authors[11,14] tried to repair the rock-salt structure to the regular layered structure. However, in the present case, the observed I_{104}/I_{003} decreases to ~85 from ~96% after the cycle tests, where the slight decrease in I_{104}/I_{003} is attributed to a small amount of deficiency of Li ions from the initial phase (Figure S9). Hence, as far as the present NCM622 is concerned, the rearrangement of the oxygen stacking sequence should be focused for efficient direct recycling. In addition, both relithiation and CEI removal are necessary to adjust the chemical composition and construct the interphase.

Finally, regarding the limitations of the present study and perspectives for realizing direct recycling, this study focused on degradation in the positive electrode (NCM622) using only the Li (half) cells. However, it is unclear how long the ~25% capacity loss in the half-cell corresponds to the actual calendar life of the full cells. The relationship between the degradation in

half and full cells should be clarified by including other durability testing methods, such as cycling at high temperatures (60 °C). Moreover, the degradation of the active material (NCM622 in this case) should be distinguished from the degradation of the entire electrode because the capacity loss observed in this study also involves the degradation of the conducting carbon and binder. The degradation mechanisms would depend on the Ni/Co/Mn composition of the positive electrode material, thereby requiring the direct recycling procedure to be tailored to the types of positive electrode materials. Indeed, *ex situ* XRD measurements on delithiated samples reveal that the NCM111 sample separates into two phases at $Q_{cha} \geq 200$ mA h g^{-1}, whereas the NCA sample maintains a single phase until 5.0 V, as for NCM622 (Figure S10). This suggests that the secondary phase as well as the stacking faults are produced in NCM111 after the cycle test at high voltages. Therefore, a trade-off relationship exists between efficiency and energy consumption when comparing direct recycling with destruction-and-regeneration-type recycling.

CONCLUSIONS

We elucidated the degradation mechanisms in Li/NCM622 cells during cycling to provide insights into the strategies for direct recycling. The delithiated NCM622 sample in the initial state could be assigned to a single phase with rhombohedral symmetry until 244 C ($x = 0.12$), and the changes in a_h and c_h were determined by the Rietveld analyses. The degradation rate rapidly increased above 4.6 V vs Li$^+$/Li or ~200 mA h g^{-1}, when the rhombohedral symmetry approached cubic symmetry because of the rapid decrease in the c_h/a_h ratio. The Q_{dis} retentions at the 30th cycle were ~95 and 75% for the cycling tests at 3.0−4.4 and 3.0−5.0 V, respectively. Cycling tests performed after the Li cells were refabricated using fresh separators and Li electrodes confirmed that the capacity fade was due to the degradation of the positive electrode.

Ex situ XRD measurements after the cycling tests clarified that no impurities were present in the NCM622 samples, such as the rock-salt NiO phase. However, selective line broadening and peak shifts were observed, indicating the formation of the stacking faults along the c_h-axis. Based on the fwhm values of the 110 diffraction peak, the amounts of stacking faults (α) were estimated to be 0.09 and 0.3 for the cycling tests at 3.0−4.4 V (150 cycles) and 3.0−5.0 V (30 cycles), respectively. Moreover, the rock-salt domains appeared on the NCM622 surface in the high-resolution TEM image both before and after cycling, although it is difficult to distinguish between the structural changes during cycling and changes caused by electron beam damage. This finding implies that the NCM622 particles degraded not at their surfaces but rather in their bulk, although structural changes on the surface were previously regarded as the main cause of degradation. This means that the bulk structure requires more attention with efficient direct recycling strategies. An annealing process would be required to rearrange the stacking into a regular sequence, and the conditions for material regeneration are currently being optimized in my research group.

ASSOCIATED CONTENT

SI **Supporting Information**

This material is available free of charge via the internet at http://pubs.acs.org/. The Supporting Information is available free of charge at https://pubs.acs.org/doi/10.1021/acsomega.3c06856.

Rietveld analysis results and structural parameters of the NCM111, NCM523, NCM811, and NCA samples; conditioning charge and discharge curves of the Li cells with NCM111, NCM523, NCM811, and NCA; Rietveld analysis results of the delithiated NCM622 samples and their structural parameters; Rietveld analysis results and structural parameters after the cycling tests at 3.0−4.2 and 3.0−4.6 V; XRD patterns enlarged near the 003, 101, and 0012 diffraction peaks; schematics of several stacking faults in the FCC structure; enlarged dark-field STEM images of the pristine and cycled samples; observed I_{104}/I_{003} before and after the cycle tests; and *ex situ* XRD patterns of the delithiated NCM111 and NCA samples (PDF)

AUTHOR INFORMATION

Corresponding Author

  Kazuhiko Mukai − *Toyota Central Research and Development Laboratories, Nagakute Aichi 480−1192, Japan;* orcid.org/0000-0002-6154-6539; Email: e1089@mosk.tytlabs.co.jp

Complete contact information is available at: https://pubs.acs.org/10.1021/acsomega.3c06856

Notes

The author declares no competing financial interest.

ACKNOWLEDGMENTS

REFERENCES

(1) Tarascon, J.-M.; Armand, M. Issues and Challenges Facing Rechargeable Lithium Batteries. *Nature* **2001**, *414*, 359−367.

(2) Winter, M.; Barnett, B.; Xu, K. Before Li Ion Batteries. *Chem. Rev.* **2018**, *118*, 11433−11456.

(3) Zheng, X.; Li, M.; El-Hady, D. A.; Alshitari, W.; Al-Bogami, A. S.; Lu, J.; Aimne, K. Commercialization of Lithium Battery Technologies for Electric Vehicles. *Adv. Energy Mater.* **2019**, *9*, 1900161.

(4) Chen, M.; Ma, X.; Chen, B.; Arsenault, R.; Karlson, P.; Simon, N.; Wang, Y. Recycling End-of-Life Electric Vehicle Lithium-Ion Batteries. *Joule* **2019**, *3*, 2622−2646.

(5) Fan, E.; Li, L.; Wang, Z.; Lin, J.; Huang, Y.; Yao, Y.; Chen, R.; Wu, F. Sustainable Recycling Technology for Li-Ion Batteries and Beyond: Challenges and Future Prospects. *Chem. Rev.* **2020**, *120*, 7020−7063.

(6) Lv, W.; Wang, Z.; Cao, H.; Sun, Y.; Zhang, Y.; Sun, Z. A Critical Review and Analysis on the Recycling of Spent Lithium-Ion Batteries. *ACS Sustain. Chem. Eng.* **2018**, *6*, 1504−1521.

(7) Harper, G.; Sommerville, R.; Kendrick, E.; Driscoll, L.; Slater, P.; Stolkin, R.; Walton, A.; Christensen, P.; Heidrich, O.; Lambert, S.; Abbott, A.; Ryder, K.; Gaines, L.; et al. Recycling Lithium-Ion Batteries from Electric Vehicles. *Nature* **2019**, *575*, 75−86.

(8) Neumann, J.; Petranikova, M.; Meeus, M.; Gamarra, J. D.; Younesi, R.; Winter, M.; Nowak, S. Recycling of Lithium-Ion Batteries-Current Sate of the Art, Circular Economy, and Next Generation Recycling. *Adv. Energy Mater.* **2022**, *12*, 2102917.

(9) Makuza, B.; Tian, Q.; Guo, X.; Chattopadhyay, K.; Yu, D. Pyrometallurgical Options for Recycling Spent Lithium-Ion Batteries: A Comprehensive Review. *J. Power Sources* **2021**, *491*, 229622.

(10) Yao, Y.; Zhu, M.; Zhao, Z.; Tong, B.; Fan, Y.; Hua, Z. Hydrometallurgical Processes for Recycling Spent Lithium-Ion

Batteries: A Critical Review. *ACS Sustain. Chem. Eng.* **2018**, 6, 13611−13627.

(11) Jiang, G.; Zhang, Y.; Meng, Q.; Zhang, Y.; Dong, P.; Zhang, M.; Yang, X. Direct Regeneration of LiNi$_{0.5}$Co$_{0.2}$Mn$_{0.3}$O$_2$ Cathode from Spent Lithium-Ion Batteries by the Molten Salts Method. *ACS Sustain. Chem. Eng.* **2020**, 8, 18138−18147.

(12) Liu, B.; Huang, J.; Song, J.; Liao, K.; Si, J.; Wen, B.; Zhou, M.; Cheng, Y.; Gao, J.; Xia, Y. Direct Recycling of Spent Li-Ni$_{0.5}$Co$_{0.2}$Mn$_{0.3}$O$_2$ Cathodes Based on Single Oxalic Acid Leaching and Regeneration under Mild Conditions Assisted by Lithium Acetate. *Energy Fuels* **2022**, 36, 6552−6559.

(13) Xu, P.; Yang, Z.; Yu, X.; Holoubek, J.; Gao, H.; Li, M.; Cai, G.; Bloom, I.; Liu, H.; Chen, Y.; An, K.; Pupek, K. Z.; Liu, P.; Chen, Z. Design and Optimization of the Direct Recycling of Spent Li-Ion Battery Cathode Materials. *ACS Sustain. Chem. Eng.* **2021**, 9, 4543−4553.

(14) Ma, J.; Wang, J.; Jia, K.; Liang, Z.; Ji, G.; Zhuang, Z.; Zhou, G.; Cheng, H.-M. Adaptable Eutectic Salt for the Direct Recycling of Highly Degraded Layer Cathodes. *J. Am. Chem. Soc.* **2022**, 144, 20306−20314.

(15) Chu, B.; Liu, S.; You, L.; Liu, D.; Huang, T.; Li, Y.; Yu, A. Enhancing the Cycling Stability of Ni-Rich LiNi$_{0.6}$Co$_{0.2}$Mn$_{0.2}$O$_2$ Cathode at a High Cutoff Voltage with Ta Doping. *ACS Sustain. Chem. Eng.* **2020**, 8, 3082−3090.

(16) Chakraborty, A.; Kunnikuruvan, S.; Kumar, S.; Markovsky, B.; Aurbach, D.; Dixit, M.; Major, D. T. Layered Cathode Materials for Lithium-Ion Batteries: Review of Computational Studies on LiNi$_{1−x−y}$Co$_x$Mn$_y$O$_2$ and LiNi$_{1−x−y}$Co$_x$Al$_y$O$_2$. *Chem. Mater.* **2020**, 32, 915−952.

(17) Tian, Y.; Zeng, G.; Rutt, A.; Shi, T.; Kim, H.; Wang, J.; Koettgen, J.; Sun, Y.; Ouyang, B.; Chen, T.; Lun, Z.; Rong, Z.; Persson, K.; Ceder, G. Promises and Challenges of Next-Generation "Beyond Li-ion" Batteries for Electric Vehicles and Grid Decarbonization. *Chem. Rev.* **2021**, 121, 1623−1669.

(18) Xu, J.; Deshpande, R. D.; Pan, J.; Cheng, Y.-T.; Battaglia, V. S. Electrode Side Reactions, Capacity Loss and Mechanical Degradation in Lithium-Ion Batteries. *J. Electrochem. Soc.* **2015**, 162, A2026−A2035.

(19) Ariyoshi, K.; Maekawa, A.; Nakamura, T. Quantification Analysis and Kinetic Modeling of Crosstalk Reactions In Lithium-Ion Batteries using a Four-Electrode Cell. *J. Electroanal. Chem.* **2022**, 916, 116383.

(20) Wang, Q.; Shen, C.-H.; Shen, S.-Y.; Xu, Y.-F.; Shi, C.-G.; Huang, L.; Li, J.-T.; Sun, S.-G. Origin of Structural Evolution in Capacity Degradation for Overcharged NMC622 via Operando Coupled Investigation. *ACS Appl. Mater. Interfaces* **2017**, 9, 24731−24742.

(21) Ryu, H.-H.; Park, K.-J.; Yoon, C.-S.; Sun, Y.-K. Capacity Fading of Ni-Rich Li[Ni$_x$Co$_y$Mn$_{1−x−y}$]O$_2$ (0.6 ≤ x ≤ 0.95) Cathodes for High-Energy-Density Lithium-Ion Batteries: Bulk or Surface Degradation? *Chem. Mater.* **2018**, 30, 1155−1163.

(22) Zhu, W.; Hovington, P.; Bessette, S.; Clément, D.; Gagnon, C.; Gariépy, V.; Provencher, M.; Mathieu, M. C.; Trudeau, M.-L.; Vijh, A.; Zaghib, K.; Kim, C. Design Parameters for Enhanced Performance of Li$_{1+x}$Ni$_{0.6}$Co$_{0.2}$Mn$_{0.2}$O$_2$ at High Voltage: A Phase Transformation Study by In Situ XRD. *J. Electrochem. Soc.* **2021**, 168, 100526.

(23) Jetybayeva, A.; Schon, N.; Oh, J.; Kim, J.; Kim, H.; Park, G.; Lee, Y.-G.; Eichel, R.-A.; Kleiner, K.; Hausen, F.; Hong, S. Unraveling the State of Charge-Dependent Electronic and Ionic Structure−Property Relationships in NCM622 Cells by Multiscale Characterization. *ACS Appl. Energy Mater.* **2022**, 5, 1731−1742.

(24) Izumi, F.; Momma, K. Three-Dimensional Visualization in Powder Diffraction. *Solid State Phenom.* **2007**, 130, 15−20.

(25) Momma, K.; Izumi, F. VESTA 3 for Three-Dimensional Visualization of Crystal, Volumetric and Morphology Data. *J. Appl. Crystallogr.* **2011**, 44, 1272−1276.

(26) Uyama, T.; Mukai, K.; Yamada, I. Synthesis of Rhombohedral LiCo$_{0.64}$Mn$_{0.36}$O$_2$ Using a High-Pressure Method. *Inorg. Chem.* **2019**, 58, 6684−6695.

(27) Li, G.; Wen, Y.; Chu, B.; You, L.; Xue, L.; Chen, X.; Huang, T.; Yu, A. Comparative Studies of Polycrystal and Single-Crystal

LiNi$_{0.6}$Co$_{0.2}$Mn$_{0.2}$O$_2$ in Terms of Physical and Electrochemical Performance. *ACS Sustain. Chem. Eng.* **2021**, 9, 11748−11757.

(28) Liu, L.; Zhang, Y.; Zhao, Y.; Jiang, G.; Gong, R.; Li, Y.; Meng, Q.; Dong, P. Surface Growth and Intergranular Separation of Polycrystalline Particles for Regeneration of Stable Single-Crystal Cathode Materials. *ACS Appl. Mater. Interfaces* **2022**, 14, 29886−29895.

(29) Chen, Z.; Lu, Z.; Dahn, J. R. Staging Phase Transitions in Li$_x$CoO$_2$. *J. Electrochem. Soc.* **2002**, 149, A1604−A1609.

(30) Duffiet, M.; Blangero, M.; Cabelguen, P.-E.; Delmas, C.; Carlier, D. Influence of the Initial Li/Co Ratio in LiCoO$_2$ on the High-Voltage Phase-Transitions Mechanisms. *J. Phys. Chem. Lett.* **2018**, 9, 5334−5338.

(31) Mukai, K.; Sugiyama, J.; Ikedo, Y.; Aoki, Y.; Andreica, D.; Amato, A. Structural and Magnetic Nature for Fully Delithiated Li$_x$NiO$_2$: Comparative Study between Chemically and Electrochemically Prepared Samples. *J. Phys. Chem. C* **2010**, 114, 8626−8632.

(32) Paterson, M. S. X-ray Diffraction by Face-Centered Cubic Crystals with Deformation Faults. *J. Appl. Phys.* **1952**, 23, 805−811.

(33) Warren, B. E.; Warekois, E. P. Stacking faults in cold worked alpha-brass. *Acta Metall.* **1955**, 3, 473−479.

(34) Yamasaki, M.; Sasaki, M.; Nishijima, M.; Hiraga, K.; Kawamura, Y. Formation of 14H Long Period Stacking Ordered Structure and Profuse Stacking Faults in Mg−Zn−Gd Alloys during Isothermal aging at High Temperature. *Acta Mater.* **2007**, 55, 6798−6805.

(35) Reynaud, M.; Serrano-Sevillano, J.; Casas-Cabanas, M. Imperfect Battery Materials: A Closer Look at the Role of Defects in Electrochemical Performance. *Chem. Mater.* **2023**, 35, 3345−3363.

(36) Casas-Cabanas, M.; Reynaud, M.; Rikarte, J.; Horbach, P.; Rodríguez-Carvajal, J. FAULTS: A Program for Refinement of Structures with Extended Defects. *J. Appl. Crystallogr.* **2016**, 49, 2259−2269.

(37) Liu, J.; Yin, L.; Wu, L.; Bai, J.; Bak, S.-M.; Yu, X.; Zhu, Y.; Yang, X.-Q.; Khalifah, P. G. Quantification of Honeycomb Number-Type Stacking Faults: Application to Na$_3$Ni$_2$BiO$_6$ Cathodes for Na-Ion Batteries. *Inorg. Chem.* **2016**, 55, 8478−8492.

(38) Mortemard de Boisse, B.; Reynaud, M.; Ma, J.; Kikkawa, J.; Nishimura, S.; Casas-Cabanas, M.; Delmas, C.; Okubo, M.; Yamada, A. Coulombic Self-Ordering upon Charging a Large-Capacity Layered Cathode Material for Rechargeable Batteries. *Nat. Commun.* **2019**, 10, 2185.

(39) Treacy, M. M. J.; Newsam, J. M.; Deem, M. W. A General Recursion Method for Calculating Diffracted Intensities from Crystals Containing Planar Faults. *Proc. R. Soc. London, Ser. A* **1991**, 433, 499−520.

(40) Mukai, K. Pseudo Zero-Strain Insertion Materials for Li-Ion Batteries: Cross-Sectional Observations of LiNi$_{1/2}$Co$_{1/2}$O$_2$, Li-Ni$_{1/3}$Co$_{1/3}$Mn$_{1/3}$O$_2$, and LiNi$_{0.8}$Co$_{0.15}$Al$_{0.05}$O$_2$. *Ionics* **2018**, 24, 2181−2186.

(41) Park, N.-Y.; Park, G.-T.; Kim, S.-B.; Jung, W.; Park, B.-C.; Sun, Y.-K. Degradation Mechanism of Ni-Rich Cathode Materials: Focusing on Particle Interior. *ACS Energy Lett.* **2022**, 7, 2362−2369.

(42) Lin, F.; Markus, I. M.; Doeff, M. M.; Xin, H. L. Chemical and Structural Stability of Lithium-Ion Battery Electrode Materials under Electron Beam. *Sci. Rep.* **2014**, 4, 5694.

(43) Ikuhara, Y. H.; Gao, X.; Kawahara, K.; Fisher, C. A.; Kuwabara, A.; Ishikawa, R.; Moriwake, H.; Ikuhara, Y. Atomic Level Changes during Electrochemical Cycling of Oriented LiMn$_2$O$_4$ Cathodic Thin Films. *ACS Appl. Mater. Interfaces* **2022**, 14, 6507−6517.

(44) Zhang, J.-N.; Li, Q.; Wang, Y.; Zheng, J.; Yu, X. Q.; Li, H. Dynamic Evolution of Cathode Electrolyte Interphase (CEI) on High Voltage LiCoO$_2$ Cathode and its Interaction with Li Anode. *Energy Storage Mater.* **2018**, 14, 1−7.

(45) Qian, H.; Ren, H.; Zhang, Y.; He, X.; Li, W.; Wang, J.; Hu, J.; Yang, H.; Sari, H. M. K.; Chen, Y.; Li, X. Surface Doping vs. Bulk Doping of Cathode Materials for Lithium-Ion Batteries: A Review. *Electrochem. Energy Rev.* **2022**, 5, 2.

(46) Park, K.-Y.; Zhu, Y.; Torres-Catanedo, C. G.; Jung, H. J.; Luu, N. S.; Kahvecioglu, O.; Yoo, Y.; Seo, J.-W. T.; Downing, J. R.; Lim, H.-D.; Bedzyk, M. J.; Wolverton, C.; Hersam, M. C. Elucidating and Mitigating

High-Voltage Degradation Cascades in Cobalt-Free LiNiO$_2$ Lithium-Ion Battery Cathodes. *Adv. Mater.* **2022**, *34*, No. e2106402.